Effect of soot particle deposition on porous fouling formation and thermal characteristics of an exhaust gas recirculation cooler

Khoshnood, Alireza; Maerefat, Mehdi; Imani, Gholamreza; Hooman, Kamel

DOI
10.1016/j.applthermaleng.2023.120629

Publication date
2023

Document Version
Final published version

Published in
Applied Thermal Engineering

Applied Thermal Engineering 229 (2023) 120629

Contents lists available at ScienceDirect

Applied Thermal Engineering

journal homepage: www.elsevier.com/locate/apthermeng

Research Paper

Effect of soot particle deposition on porous fouling formation and thermal characteristics of an exhaust gas recirculation cooler

Alireza Khoshnood [a], Mehdi Maerefat [a], Gholamreza Imani [b,*], Kamel Hooman [c]

[a] Department of Mechanical Engineering, Tarbiat Modares University, Tehran, Iran
[b] Department of Mechanical Engineering, Persian Gulf University, 75169 Bushehr, Iran
[c] Department of Process and Energy, Delft University of Technology, Leeghwaterstraat 39, 2628 CB Delft, the Netherlands

ARTICLE INFO

Keywords:
Exhaust gas recirculation cooler
Particle deposition
Evolving porous fouling layer
Thermophoresis
Steady fouling layer
Lattice Boltzmann method

ABSTRACT

Exhaust gas recirculation (EGR) systems have been successfully employed to reduce the NOx emissions in diesel engines. However, the fouling problem in EGR coolers challenges their capability to comply with stringent environmental regulations. A few numerical simulations have considered the fouling growth in EGR coolers. Those studies modeled the evolving fouling layer to be a solid medium, therefore, fluid flow and convection heat transfer within the fouling layer, which is well-documented to be a porous medium permeable to gas flow, have not been considered yet. As such, the present study investigates the simultaneous effects of the formation of the evolving porous fouling layer (EPFL) at the walls of an EGR cooler and fluid flow and convection heat transfer simulation within this EPFL to determine its coupled effects on the thermal performance of the EGR cooler. This study also investigates the possibility of formation of a steady fouling layer (SFL) because of the opposing effects of the fouling layer growth and deposition rate. The effects of two pertinent dimensionless parameters, namely Darcy number ($10^{-4} \leq Da \leq 5 \times 10^{-3}$) and Reynolds number ($100 \leq Re \leq 400$) on the time history of the fouling layer growth, deterioration of the thermal performance of the duct, and average Nusselt number ratio ($Nu_{av}/Nu_{av}(t=0)$) are studied. The results show that the thermal performance of the duct decreases as the EPFL grows, which agrees well with the available experimental data. It is shown that the steady fouling layer is obtained due to a decrease in thermophoretic force and deposition rate, as a result of the EPFL formation. Finally, a correlation is proposed in terms of Reynolds and Darcy numbers for the time at which the SFL occurs.

1. Introduction

Exhaust gas recirculation (EGR) systems are developed to reduce NOx emissions in diesel engines. This reduction in NOx emissions is accomplished by lowering the combustion temperature through cooling down a portion of exhaust gas in an EGR cooler and recirculating it into the engine manifold [1,2]. However, the fouling problem in EGR coolers has been an engineering challenge ever since those systems have been introduced. It has been shown that the fouling in EGR coolers reduces their thermo-hydraulic performance over time [3–6]. Numerous studies have been devoted to investigating this problem during the previous two decades. The majority of the research has been conducted either experimentally or numerically.

Many experimental studies have been done to shed some light on the fouling mechanism in EGR coolers. It was shown that the fouling in EGR coolers is developed mainly due to the deposition of soot particles and condensation of soluble organic fractions (SOF) [7]. However, Hong et al. [8] experimentally showed that for a coolant temperature of 353 K, which is common in EGR coolers, the effect of SOF condensation on the fouling was negligible. They explained that for this coolant temperature, a very small amount of SOF condensed on the cooler wall, therefore its effect on the fouling was negligible. Therefore, according to the available research, fouling in EGR coolers is mainly caused by the deposition of soot particles [9]. Bika et al. [10] measured the soot particle size and concentration upstream and downstream of a heat exchanger to evaluate the particulate matter deposition rate. Their findings revealed that the hydrocarbon condensation had a negligible effect on particle deposition. Although different mechanisms such as thermophoretic force, diffusion, inertial impact, and gravitational settling are shown to be involved in EGR coolers fouling, many studies reported that this phenomenon is mostly caused by the thermophoretic force exerted on nano-

* Corresponding author.
E-mail addresses: a.khoshnood@modares.ac.ir (A. Khoshnood), maerefat@modares.ac.ir (M. Maerefat), g.r.imani@pgu.ac.ir (G. Imani), K.hooman@TUDelft.nl (K. Hooman).

https://doi.org/10.1016/j.applthermaleng.2023.120629
Received 2 January 2023; Received in revised form 31 March 2023; Accepted 17 April 2023
Available online 22 April 2023

Nomenclature

C	lattice velocity
C_s	speed of sound
Da	Darcy number, $K/(2H)^2$
d_p	particle diameter
EPFL	evolving porous fouling layer
FPL	fixed porous layer
e	dimensionless porous layer thickness, $e = 2\delta/H$
$\boldsymbol{e}_i$	discrete velocity
$\boldsymbol{F}$	total resistant force (N)
F_D	drag force
f_i	density distribution function
f_i^{eq}	equilibrium density distribution function
f_i^{neq}	non-equilibrium density distribution function
$\boldsymbol{F}_{SL}$	Saffman lift force
$\boldsymbol{F}_{th}$	thermophoresis force
F_ε	geometrical function
g_i	temperature distribution function
g_i^{eq}	equilibrium temperature distribution function
H	width of the duct (m)
K	permeability of the porous layer (m^2)
k_f	fluid thermal conductivity
Kn	Knudsen number
k_p	particle thermal conductivity
L	length of the duct (m)
l_g	length of the grid (m)
m_p	particle mass (kg)
n_{in}	number of injected particles every time step
n_{cr}	critical number of deposited particles
Nu_{fd}	fully developed Nusselt number
Nu_{av}	average Nusselt number
Nu_L	local Nusselt number
Nu_r	Nusselt number ratio
Pr	Prandtl number, ν_f/α_f
Re	Reynolds number, $\rho\overline{U}_{in}(2H)/\nu_f$
S_{in}	the cross-sectional area of the inlet (m^2)
SFL	steady fouling layer
t	elapsed time (s)
t_{SFL}	steady fouling layer time (s)
T	temperature (K)
T_b	bulk temperature (K)
$T_{b,out}$	bulk temperature at the outlet (K)
T^{eq}	equilibrium temperature (K)
T_{in}	inlet temperature (K)
T_{out}	outlet temperature (K)
T_w	wall temperature (K)
u	fluid horizontal velocity (ms^{-1})
$\boldsymbol{u}_p$	particle velocity (ms^{-1})
$\overline{U}_{in}$	average inlet fluid velocity (ms^{-1})
$\boldsymbol{V}$	temporal velocity vector (ms^{-1})
x	longitudinal coordinate (m)
X	dimensionless longitudinal coordinate (x/H)
y	vertical coordinate (m)
Y	dimensionless vertical coordinate (y/H)

Greek symbols

α_e	effective thermal diffusivity (m^{2}s^{-1})
α_f	fluid thermal diffusivity (m^{2}s^{-1})
Δt_r	real time step (s)
δ	FPL thickness (m)
δx	lattice spacing (m)
δ_t	time step (s)
ε	porosity
η	Talbot coefficient
ν_e	effective kinematic viscosity (m^{2}s^{-1})
ν_f	fluid kinematic viscosity (m^{2}s^{-1})
ρ	fluid density (m^{3}kg^{-1})
ρ_p	particle density (m^{3}kg^{-1})
μ_f	fluid viscosity
τ_t	dimensionless temperature relaxation time
τ_v	dimensionless velocity relaxation time
ω_i	weighting coefficients

sized particles due to temperature gradients [11–13]. Malayeri et al. [13] experimentally investigated the effect of thermophoretic force by varying the temperature gradient between hot particles and the cold surface of an EGR cooler. Their findings indicated that the fouling rates increased for higher temperature gradients.

Numerous studies experimentally investigated the effects of different parameters on the effectiveness of EGR coolers [14–17]. Hoard et al. [14] experimentally investigated the effect of the Reynolds number on effectiveness of an EGR cooler. They reported that the effectiveness was dropped when Reynolds number was increased. Jang et al. [15] performed a series of experiments to measure the time history of the effectiveness of wave fin-type EGR coolers for different wave and fin pitches to find the best geometry in terms of cooler effectiveness. Park et al. [17] experimentally investigated the thermal efficiency drop in low-flow EGR coolers with varying coolant temperatures. They observed that a decrease in the coolant temperature led the deposition layer to grow more, which in turn caused a higher drop in thermal efficiency. Experimental studies showed that the fouling layer thickness finally reaches a steady state condition called the asymptotic behavior of fouling layer, after which the effectiveness of the EGR cooler does not vary with time [6,11,13,16]. Many authors attributed this phenomenon to opposing effects of fouling layer growth and deposition in combination with the removal mechanism. Ebd-Elhadi and Malayeri [6] explained that when the fouling layer thickness increases during the initial stage of deposition, the thermal resistance that this layer offers increases, which in turn decreases the particle deposition rate. On other hand, an increase in the fouling layer thickness increases the flow velocity due to a decrease in the duct cross-section, which consequently increases the removal rate of the deposit. They concluded that the asymptotic behavior of the fouling layer occurs due to a balance between decreasing deposition rate and increasing removal rate.

Numerical studies in addition to experimental research have been done for a better understanding of the fouling phenomenon and its effect on the thermo-hydraulic performance of the EGR coolers. A few numerical studies have investigated the fouling layer growth by simulating the particle deposition. Generally, two approaches have been followed to model the fouling layer growth in EGR coolers. In the first approach, fluid cells are converted into *solid* ones after a predefined condition is met, which can be the maximum number of particles allowed to deposit in a cell. The second approach, on other hand, recreates the fouling growth using the dynamic mesh, where the position of the nodes on the fluid-fouling interface is updated at each time. It should be emphasized that in the second approach the growing fouling layer is also considered to be a solid medium [18]. Paz et al. [19] employed the first approach to study the evolution of solid fouling layer thickness in an EGR cooler with reasonable agreement obtained compared to available experimental data. Abarham et al. [20] suggested a 2-D axisymmetric model based on the second approach in which the thickness of the solid deposit was adjusted by changing the fouling-fluid interface. They estimated the evolution of the solid fouling layer at each time step of the simulation. Tong et al. [21] followed the second approach to investigate the real-time simulation of the solid fouling layer growth in a heat recovery boiler. They magnified the simulation time step to be able to achieve higher operation times for the fouling process, which can be hours or even days. Their findings demonstrated a constant fouling growth rate without addressing the removal process. After the removal condition was added to their work, the fouling layer reached a steady state thickness called asymptotic behavior of the fouling layer or steady fouling layer (SFL) here. Tang et al. [22] used the second approach to study the morphology prediction of heat exchangers with a real-time simulation of the solid fouling layer growth with Ansys Fluent. They also followed the same procedure as Ref. [21] to magnify the simulation time. However, according to experimental data, the fouling in EGR coolers is reported to be a porous layer with a porosity of 0.98 and thermal conductivity of 0.041W/mK [23], which is permeable to the EGR flow. The effect of fluid flow and convection heat transfer within the porous fouling layer has not been considered yet.

The numerical modeling of fluid flow and heat transport in porous media has received much attention [24–25] due to the broad engineering applications of the problem. The lattice Boltzmann method (LBM) has been used for simulating heat transfer and fluid flow in porous media for the past two decades due to some inherent features such as high compatibility with complex geometries and easy parallelization of the code, to name a few [26–27]. The effect of partial porous layers on the hydrodynamic and thermal characteristics of a duct carrying a fluid has been investigated using the LBM. Shokouhmand et al. [28–29] used the LBM to study the effect of fixed porous layers (FPL) on the forced convection heat transfer from a parallel-plate duct. They considered two configurations of the porous layers; one at the walls and the other at the core of the duct. In their study, the results showed good agreement with the available experimental data. Khoshnood et al. [30] numerically investigated the effect of evolving porous layers in a parallel plate duct on the thermal convection of the duct. They employed the LBM to simulate the fluid flow and heat transfer in a duct with evolving porous layers at the walls. They demonstrated that the porous layers did not significantly affect the thermal performance of the duct before a certain time, which they called it the *evolution time*.

To the best of the authors' knowledge, in studies that considered the numerical simulation of the fouling growth of EGR coolers, the fouling layer was considered to be *impermeable*. Therefore, the effects of fluid flow and convection heat transfer within the fouling layer were neglected. However, as mentioned in the above literature survey, in real applications, the EGR fouling is shown to be a porous medium that is permeable to EGR flow. Thus, the effect of fluid flow and convection heat transfer within this porous layer needs to be investigated on the fouling layer growth and thermal performance of the EGR cooler. This study aims at investigating the thermo-hydraulic effect of the evolving porous fouling layer (EPFL) on the possibility of developing SFL (i.e., the asymptotic behavior of the fouling layer) in an EGR cooler without considering the removal mechanism. As such, the numerical simulation of the particle-laden flow with transient forced convection heat transfer in a parallel-plate duct, which resembles one passage of an EGR cooler, is considered, where the deposition of the soot particles occurs at the walls mainly due to the thermophoretic force thereby building up an evolving porous fouling layer (EPFL). In this study, the effects of Reynolds number and dimensionless permeability (i.e., Darcy number) of the EPFL on the time-histories of the fouling layer profile and deterioration of the thermal performance are studied. The LBM is used based on some inherent features such as easy coding and easy parallelization of the algorithm, which is vital for numerical simulation of the fouling growth in real-world EGR coolers due to the high computational costs of such problems.

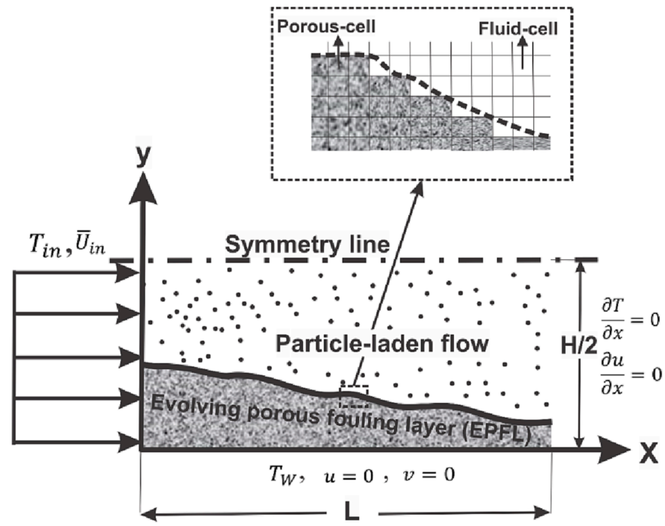

Fig. 1. The schematic of the problem.

2. The mathematical model

2.1. Geometry and problem description

Fig. 1 schematically shows the geometry of the problem and the particle-laden flow with an EPFL forming at the wall of the duct of an EGR cooler. The following assumptions are made in modeling the problem described in Fig. 1.

I. A hydrodynamically fully developed flow with uniform temperature enters the cooler duct.

II. The flow regime is considered to be laminar, which is for the case of low-flow EGR. This assumption is justified based on the available experimental works [10,14].

III. Due to the large heat capacity of coolant compared to that of EGR flow, the walls are considered to be at a constant temperature T_w [31].

IV. The exhaust gas is assumed to contain only soot particles and condensation of SOF is neglected which is justifiable for large wall temperatures [8].

V. The removal mechanism is ignored because of the low-flow EGR considered [4,11].

VI. The thermophoresis is considered as the dominant mechanism for deposition of nano-sized soot particles [11–13].

VII. The one-way interaction between the fluid flow and particles is considered due to the small size and low concentration of particles in EGR coolers [32,33].

2.2. Governing equations

The problem described in Fig. 1 includes transient fluid flow and convection heat transfer in a parallel-pate duct partially being filled by an EPFL due to the deposition of particles at the wall. For modeling the fluid flow and convection heat transfer within the EPFL, in this paper, the LBM proposed by Wang et al. [34] is employed based on the intrinsic phase averaging of the Brinkman-Forchheimer extended Darcy equation. Moreover, following the one-domain approach, the LBM governing equations for the fluid flow and convection heat transfer within the EPFL are used for the homogeneous fluid medium as well. The only modification is that the porosity and permeability of the porous medium are, respectively, chosen to be equal to one and a sufficiently large value, to resemble the homogeneous fluid medium. The problem also includes modeling the particle motion, deposition, and EPFL formation. In what follows, the LBM for fluid flow and convection heat transfer in the partial porous geometry described in Fig. 1, as well as modeling particle motion, deposition, and EPFL formation are presented.

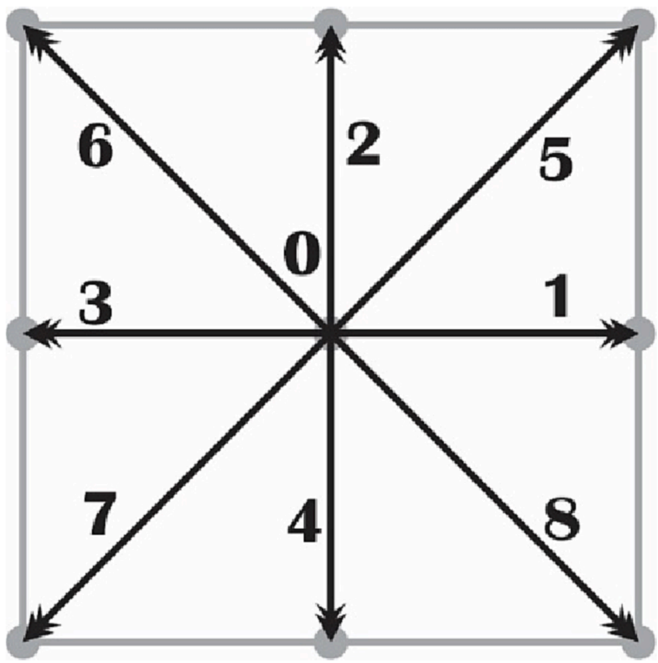

Fig. 2. The schematic of the D_2Q_9 lattice model.

2.2.1. LBM for fluid flow modeling in a partially porous media

Lattice Boltzmann method for fluid flow modeling in porous media uses the following evolution equation for density distribution function [34]:

$$f_i(\boldsymbol{r}+\boldsymbol{e}_i\delta t, t+\delta t) - f_i(\boldsymbol{r}, t) = \frac{f_i^{eq}(\boldsymbol{r}, t) - f_i(\boldsymbol{r}, t)}{\tau_v} + \delta t F_i \quad , \quad (\mathrm{i} = 0-8)(1)$$

where f_i is the density distribution function, t is time, δt is the time step, i denotes the discrete microscopic velocity directions, $\boldsymbol{e}_i$ is the discrete microscopic velocity vector, F_i is the discrete body force, and τ_v is the dimensionless hydrodynamic relaxation time. For the D_2Q_9 lattice model (i.e., two-dimensional with nine microscopic velocities) used in the present study (see Fig. 2), $\boldsymbol{e}_i$ is defined as follows [34]:

$$\boldsymbol{e}_i = \begin{cases} 0; i = 0 \\ \cos[(i-1)\pi/4)], \sin[(i-1)\pi/4)]C; i = 1-4 \\ \sqrt{2}\cos[(i-1)\pi/4)], \sin[(i-1)\pi/4)]C; i = 5-8 \end{cases} \tag{2}$$

where $C = \delta x/\delta t$ is the lattice streaming speed, which is equal to 1 in the present study.

the equilibrium distribution function that appeared in equation (1) is defined as follows [34]:

$$f_i^{eq} = \omega_i \rho \left[1 + \frac{\boldsymbol{e}_i \bullet \boldsymbol{u}}{C_s^2} + \frac{(\boldsymbol{e}_i \bullet \boldsymbol{u})^2}{2C_s^4} - \frac{\boldsymbol{u} \bullet \boldsymbol{u}}{C_s^2}\right] \quad , \quad (\mathrm{i} = 0, \cdots, 8) \tag{3}$$

where ω_i are lattice weight coefficients that for the D_2Q_9 lattice model are given as $\omega_0 = 4/9$, $\omega_{1-4} = 1/9$, and $\omega_{5-8} = 1/36$, C_s is the lattice sound speed that is equal to $1/\sqrt{3}$ for the D_2Q_9 lattice model, and $\boldsymbol{u}$ and ρ are macroscopic velocity and fluid density, respectively.

The discrete body force F_i appeared on the right-hand side of equation (1) is defined as follows [34]:

$$F_i = \omega_i \rho \left(1 - \frac{1}{2\tau_v}\right) \left[\frac{\boldsymbol{e}_i \bullet \boldsymbol{F}}{C_s^2} + \frac{\boldsymbol{uF} : \boldsymbol{e}_i\boldsymbol{e}_i}{C_s^4} - \frac{\boldsymbol{u} \bullet \boldsymbol{F}}{C_s^2}\right] \quad , \quad (\mathrm{i} = 0, \cdots, 8) \tag{4}$$

where $\boldsymbol{F}$ is the macroscopic force that resists the fluid flow through porous media, which comprises viscous (i.e., Darcy) and form (i.e., Forchheimer) drags, respectively, as follows [34]:

$$\boldsymbol{F} = -\frac{\varepsilon \nu_f}{K}\boldsymbol{u} - \frac{\varepsilon^2 F_\varepsilon}{\sqrt{K}}\boldsymbol{u}|\boldsymbol{u}| \tag{5}$$

where ε is the porosity of the porous medium, ν_f is the fluid kinematic viscosity, K is the permeability of the porous medium, and F_ε is a geometrical function given by Ergun's correlation as $F_\varepsilon = 1.75/\sqrt{(150\varepsilon^3)}$.

the macroscopic density and velocity are calculated as follows:

$$\rho = \sum_{i=0}^{8} f_i; \rho\boldsymbol{u} = \sum_{i=0}^{8} f_i \boldsymbol{e}_i + \frac{\delta t}{2}\rho\boldsymbol{F} \tag{6}$$

as can be seen in equation (6), $\boldsymbol{u}$ cannot be calculated explicitly because $\boldsymbol{F}$ comprises linear and quadratic terms in $\boldsymbol{u}$ (see equation (5)); therefore, $\boldsymbol{u}$ is calculated as follows:

$$\boldsymbol{u} = \frac{\boldsymbol{V}}{C_0 + \sqrt{C_0^2 + C_1|\boldsymbol{V}|}} \tag{7}$$

where $\boldsymbol{V}$ is a temporal velocity defined as $\rho\boldsymbol{V} = \sum_{i=0}^{8} f_i \boldsymbol{e}_i$ and C_0 and C_1 are two constants calculated as follows, respectively [34]:

$$C_0 = \frac{1}{2}\left(1 + \varepsilon\frac{\delta t}{2}\frac{\nu_f}{K}\right) \tag{8}$$

$$C_1 = \varepsilon^2 \frac{\delta t}{2}\frac{F_\varepsilon}{\sqrt{K}} \tag{9}$$

the Darcy number is defined as follows:

$$Da = \frac{K}{(2H)^2} \tag{10}$$

where H is the width of the duct.

for small Mach numbers, the Chapman-Enskog analysis recovers the following generalized Navier-Stokes equation from equations (1)-(5):

$$\nabla \bullet \boldsymbol{u} = 0 \tag{11}$$

$$\frac{\partial \boldsymbol{u}}{\partial t} + (\boldsymbol{u} \bullet \nabla)(\boldsymbol{u}) = -\frac{1}{\rho}\nabla(p) + \nu_e \nabla^2 \boldsymbol{u} + \boldsymbol{F} \tag{12}$$

where p is the fluid pressure $(p = \rho C_s^2)$, ν_e is the effective kinematic viscosity of the porous medium given as $\nu_e = C_s^2(\tau_v - 0.5)\delta t$ considered to be equal to the fluid kinematic viscosity ν_f.

As seen before in Fig. 1, the EPFL partially fills the duct; thus, the geometry of the problem comprises the porous and adjacent homogeneous fluid media. Therefore, the fluid flow also needs to be simulated in the homogeneous fluid medium. As mentioned before, in the present study, the one-domain approach is invoked where the homogeneous fluid medium is considered to be a porous medium with porosity equal to 1 and Darcy number equal to a sufficiently large value of 10^{20}. This way, one set of governing equations is needed for both porous and homogeneous fluid media.

2.2.2. LBM for convection heat transfer modeling in partially porous media

The following LBM equation describes the evolution of the temperature distribution function [28,35]:

$$g_i(\boldsymbol{r}+\boldsymbol{e}_i\delta t, t+\delta t) - g_i(\boldsymbol{r}, t) = \frac{g_i^{eq}(\boldsymbol{r}, t) - g_i(\boldsymbol{r}, t)}{\tau_t} \quad , \quad (\mathrm{i} = 0, \cdots, 8) \tag{13}$$

where g_i is the temperature distribution function and τ_t is dimensionless temperature relaxation time given as $\tau_t = ((\tau_v - 0.5)/\mathrm{Pr}) + 0.5$, where Pr is the Prandtl number. The temperature equilibrium distribution function is defined as follows [28,35]:

$$g_i^{eq} = \omega_i T\left[1 + \frac{\boldsymbol{e}_i \bullet \boldsymbol{u}}{C_s^2}\right] \tag{14}$$

where T is the macroscopic temperature defined as $T = \sum_i g_i$.

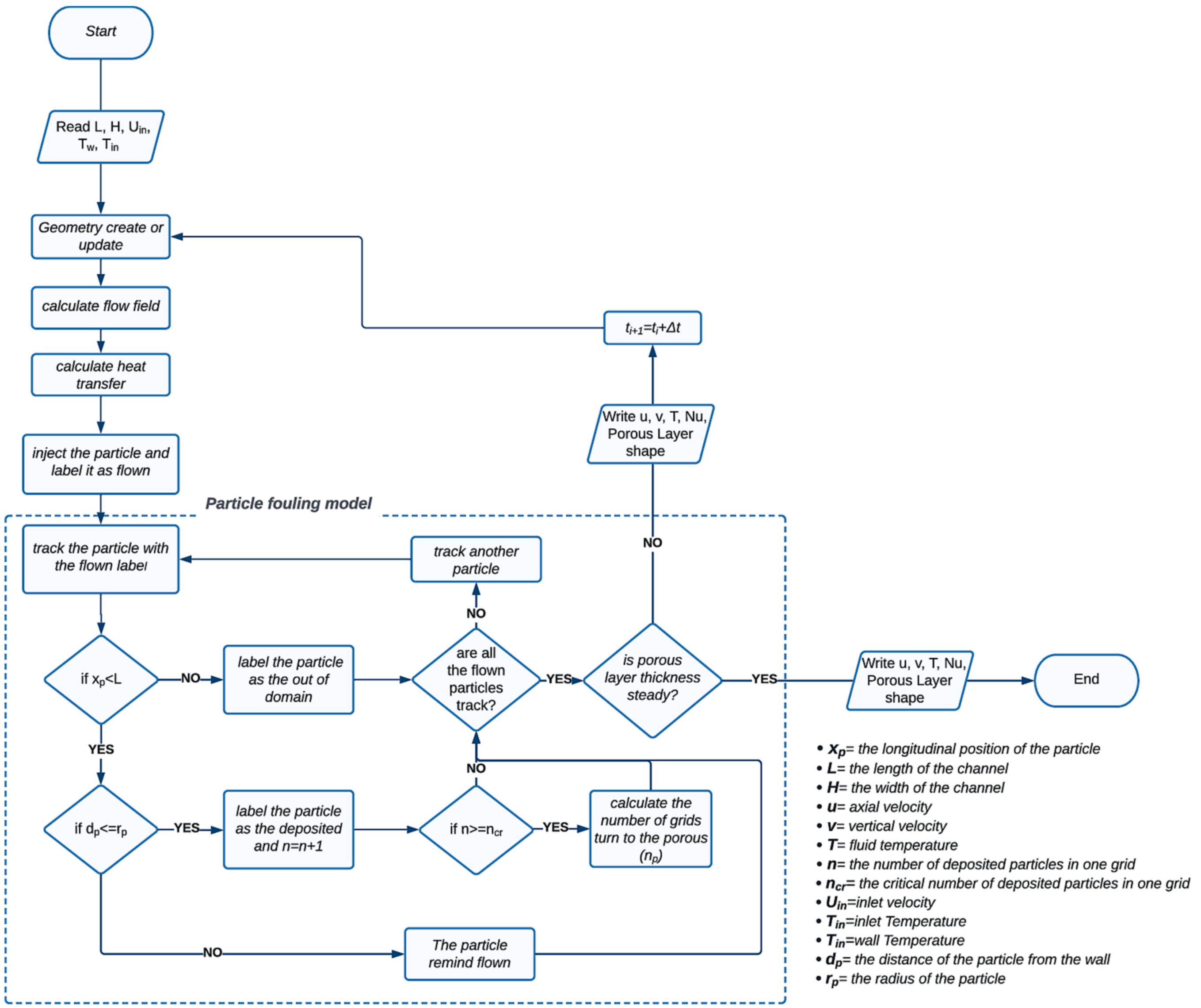

Fig. 3. The flowchart of the fouling growth simulation.

Similar to the fluid flow simulation, here also, the one-domain approach is used to simulate the convection heat transfer in the parallel-plate duct with EPFL created at the wall by particle deposition. In the one-domain approach, the homogeneous fluid adjacent to the porous medium is considered to be a fictitious porous medium with porosity equal to 1 and the Darcy number equal to a sufficiently large value of 10^{20}. This way, a single energy equation can be considered for simulating heat convection in both porous and homogeneous fluid media. The local thermal equilibrium model (LTE) is assumed since the thermal conductivity of fluid is significantly close to the porous fouling layer in EGR cooler systems [36]. So, the volume-averaged macroscopic energy equation with LTE assumption is recovered from equations (13)-(14) as follows:

$$\frac{\partial T}{\partial t}+\boldsymbol{u}\bullet\nabla\mathrm{T}=\nabla\bullet(\alpha_e\nabla T) \tag{15}$$

where $\alpha_e=C_s^2(\tau_t-0.5)\delta t$ is the effective thermal diffusivity of the porous medium assumed to be equal to that of fluid denoted by α_f in the present study.

2.2.3. Boundary conditions

The macroscopic hydrodynamic and thermal boundary conditions shown in Fig. 1 must be translated into the mesoscopic framework of LBM. The current study uses the Zuo-He method to convert the fully developed inlet and outlet velocities into the LBM framework [37]. The non-equilibrium extrapolation approach proposed by Guo et al. [38] is used to enforce the no-slip condition at the lower wall of the duct. The counter-slip approach proposed by D'Orazio et al. [39] is used to apply the constant temperature boundary condition at the inlet and lower wall and the zero-temperature gradient at the outlet. At the upper wall of the duct, symmetry conditions are applied. More explanations of the mentioned conditions are given in our previous study [30].

2.2.4. Particle motion and deposition

In this section, the forces affecting the deposition of particles and the formation of EPFL are introduced. The motion of each particle is described by Newton's second law as follows [40,41]:

$$m_p\frac{d\boldsymbol{u}_p}{dt_p}=\boldsymbol{F}_D+\boldsymbol{F}_{SL}+\boldsymbol{F}_{Th} \tag{16}$$

where m_p is the mass of each particle, $\boldsymbol{u}_p=d\boldsymbol{x}_p/dt_p$ is the particle velocity, dt_p is the time step of the particle motion, $\boldsymbol{F}_D$ and $\boldsymbol{F}_{SL}$ are the drag and lift that develop due to the velocity slip between each particle and fluid flow, respectively, and $\boldsymbol{F}_{Th}$ is the thermophoresis force that arises due to the temperature gradient within the fluid medium.

The drag force is defined as [40]:

$$\boldsymbol{F}_D = (\frac{3m_p}{4}C_D C_{cun}(\boldsymbol{u}-\boldsymbol{u}_p)|\boldsymbol{u}-\boldsymbol{u}_p|)/d_p \tag{17}$$

where $C_D = (24/Re_p)(1+0.15Re_p^{0.687})$ is the drag coefficient, $Re_p = \rho(|\boldsymbol{u}-\boldsymbol{u}_p|)d_p/\mu$ is the particle Reynolds number, $\boldsymbol{u}$ and $\boldsymbol{u}_p$ are fluid and particle velocities, $C_{cun} = 1 + Kn(1.257+0.4e^{-1.1/Kn})$ is the Cunningham coefficient, d_p is the particle diameter, and Kn is the Knudsen number defined as [41]:

$$Kn = \frac{2\lambda}{d_p} \tag{18}$$

where λ is the mean free path of the fluid molecules.

The Saffman lift is taken as follows [40,41]:

$$\boldsymbol{F}_{SL} = 1.61\times\left((\mu_f\rho)^{1/2}d_p^2(\boldsymbol{u}-\boldsymbol{u}_p)\left|\frac{\partial u}{\partial y}\right|^{1/2}\right) \tag{19}$$

where μ_f is the fluid dynamic viscosity, ρ is the fluid density, u is the horizontal component of the fluid velocity.

As the high gradient temperature exists in EGR coolers, thermophoresis force plays an essential role in particle motion in such systems [12,41] described mathematically as follows:

$$\boldsymbol{F}_{Th} = -\eta\nabla\ln T \tag{20}$$

where η is the Talbot coefficient defined as follows [41]:

$$\eta = \frac{2C_s'\left(\frac{k_f}{k_p}+C_t Kn\right)C'}{(1+3C_m Kn)\left(1+\frac{2k_f}{k_p}+2C_t Kn\right)} \tag{21}$$

where k_f and k_p are fluid and particle thermal conductivity, respectively, and C_m, C_s', C', C_t are constant coefficients obtained from experiments [41].

2.2.5. Fouling growth model

Since the time step of fluid flow simulation is too small due to stability issues, it is nearly impossible to simulate the whole fouling time duration, which can be hours or even days, with reasonable computational costs. Thus, the simulation time step is magnified in the present study as follows [42]:

$$\Delta t_r = \frac{l_g n_{in}\varphi\rho_p\delta_{cr}}{C_r n_{cr}\overline{U}_{in}S_{in}} \tag{22}$$

where Δt_r is the magnified time step, l_g is the length of the grid, which is equal to the lattice spacing δx, n_{in} is the number of particles that enter the domain every time step, which is taken equal to 1 in the present study, $\varphi = 1-\varepsilon$, ε is the porosity of the fouling layer, n_{cr} is the number of particles that need to deposit in a cell based on the given porosity, and δ_{cr} is equal to the height of the grid (lattice spacing), C_r is the real mass concentration of particles, $\overline{U}_{in}$ is the average inlet velocity, and S_{in} is the cross-sectional area of the inlet. The flowchart of the fouling growth model is shown in Fig. 3. The particles are injected into the domain randomly from the inlet where they can deposit on the wall of the duct. If the number of deposited particles in one cell reaches the critical number n_{cr}, the fluid cell changes to the porous cell, which act as a porous medium for the fluid and an impermeable block for upcoming particles such that particles can only deposit on the faces of this cell, building up more porous cells.

2.2.6. Nusselt number

In the present study, the Nusselt number is calculated to study the time history of the thermal performance of the duct and investigate the EPFL growth as well as the time at which the EPFL thickness reaches its steady value. The local Nusselt number is defined as follows [43]:

Table 1
Simulation parameters.

Parameters	Value
$Re = \rho\overline{U}_{in}(2H)/\nu_f$	$100, 200, 400$
$Pr = \nu_f/\alpha_f$	0.74
T_{in}	673(K)
T_w	353(K)
ε	0.98
$Da = K/(2H)^2$	$10^{-4}, 5\times10^{-4}, 10^{-3}, 5\times10^{-3}$
H	$0.001m$
L	$5H$

Table 2
Particle simulation parameters.

Parameters	Value
d_p	200(nm)
C_r	$2\times10^{-6}(\mathrm{kg/m^3})$
ρ_p	$2000(\mathrm{kg/m^3})$
K_n	0.02

$$Nu_L(x,t) = -2H\left(\frac{\partial T(x,y,t)}{\partial y}\right)_{x,y=0}/(T_W - T_b(x)) \tag{23}$$

where $T_b(x)$ is the computed bulk temperature at each longitudinal position x of the duct. The local Nusselt number is averaged over the duct length to obtain the average Nusselt number, which is then used to analyze the overall heat transfer performance of the duct with EPFL generated from particle deposition, taking both thermal entry and fully developed regions into account:

$$Nu_{av}(t) = \frac{1}{L}\int_0^L Nu_L(x,t)dx \tag{24}$$

3. Numerical simulation

The lattice Boltzmann method is used to simulate the fouling layer formation due to the particle deposition in a parallel-plate duct (see Fig. 1). This phenomenon occurs in EGR coolers, developed to reduce the NOx emission generated by diesel engines. Table.1 shows the simulation parameters, including Reynolds number, Prandtl number, inlet temperature, wall temperature, porosity, Darcy number, duct width, and duct length (Re, Pr, T_{in}, T_w, ε, Da, H, and L, respectively) [12,14]. The distribution of the particles in the exhaust of a diesel engine shows that the majority of soot particles have $d_p = 200\mathrm{nm}$ [44] with soot density of $\sim 2000\,\mathrm{kg/m^3}$ [45]. Moreover, the particle simulation parameters, including the diameter of the particle, particle mass concentration, particle density, and Knudsen number (d_p, C_r, ρ_p, Kn, respectively), are presented in Table 2.

The porous fouling layer (EPFL) grows by changing fluid cells to porous ones after the deposited particles reach the priorly known critical number in each cell, n_{cr}, which is checked at every time step. After that, the EPFL geometry is updated, and the hydrodynamic and thermal effects of these generated porous layers are taken into account by simulating the fluid flow and convection heat transfer within the updated EPFL (see Fig. 3).

3.1. Grid study

To perform the grid study, the LBM simulation of the steady forced convection heat transfer in a parallel-plate duct with two FPLs at the walls is considered for $Da = 5\times10^{-3}$, $Re = 400$, and dimensionless porous layer thickness $e = 0.3$. The problem is simulated using four grids, namely 26×251, 51×501, 101×1001, and 201×2001. As

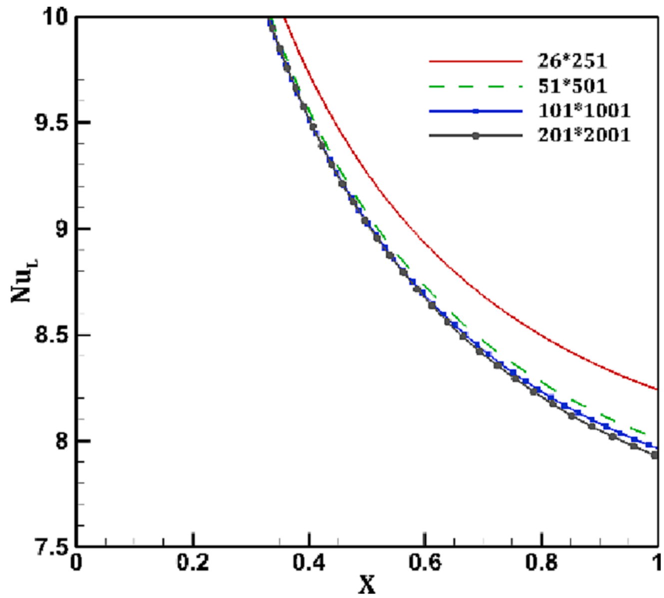

Fig. 4. The results of the local Nusselt number for $Da = 5 \times 10^{-3}$, $Re = 400$, and $e = 0.3$.

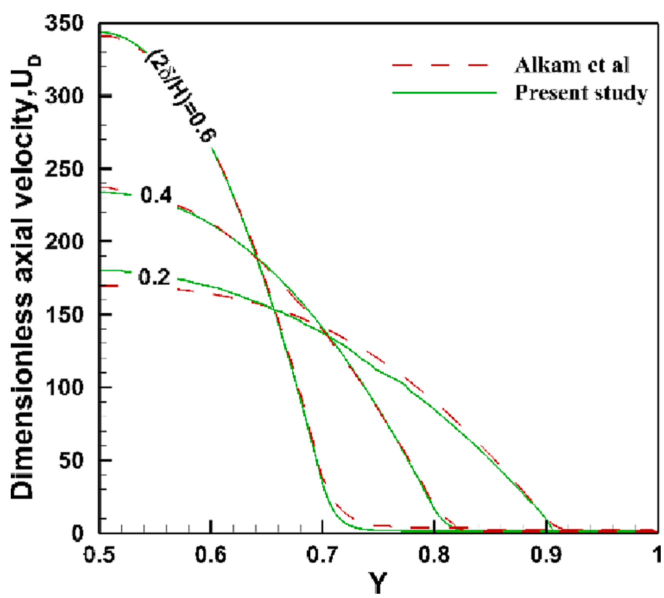

Fig. 5. Validation of dimensionless axial velocity profile against dimensionless vertical coordinate for various FPL thicknesses at $X = 2$.

shown in Fig. 4, the results of the local Nusselt number for grids 101×1001 and 201×2001 are almost indistinguishable. Therefore, grid 101×1001 is chosen for all the simulations in the present study.

3.2. Validation

Two case studies are designed to validate the LBM FORTRAN code developed in this study. The first one is designed for verifying the code for fluid flow and convection heat transfer simulations in partially porous ducts and the second one for verifying the fouling growth modeling. The first case study considers the steady convection heat transfer in a parallel-plate duct with two FPLs at the walls for $Re = 200$ and different values of the FPL dimensionless thickness. In Fig. 5, the results of the dimensionless axial velocity profile ($U_D = uH/\nu_f$) for different dimensionless FPL thicknesses at $X = 2$ are compared with

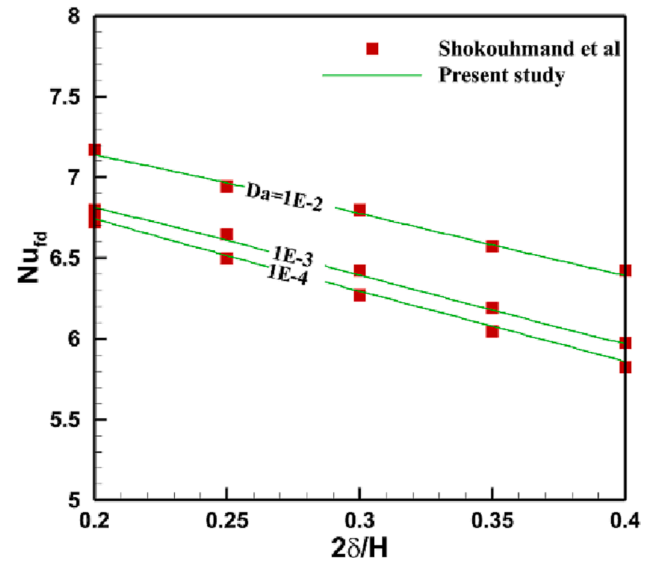

Fig. 6. Validation of the fully developed Nusselt number versus dimensionless FPL thickness for different Darcy numbers.

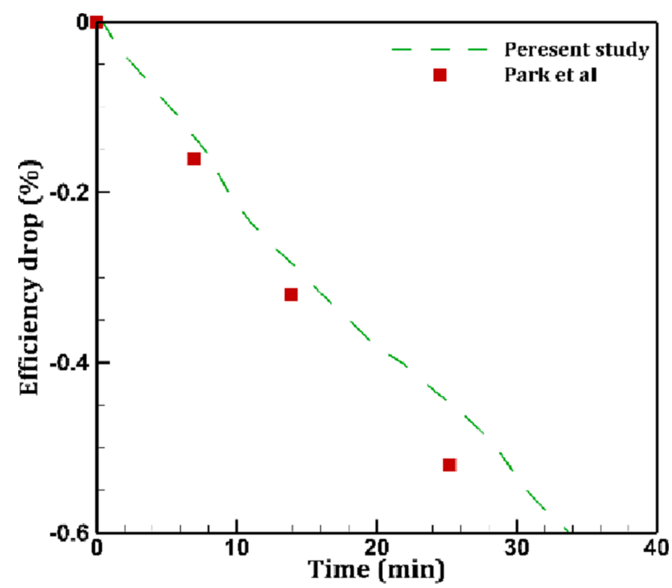

Fig. 7. Validation of the thermal effectiveness reduction over time with that of a real EGR duct.

those of Alkam et al. [46] and good agreement is observed. Moreover, in Fig. 6, the fully developed Nusselt number, Nu_{fd} versus dimensionless FPL thickness is compared with that of Shokouhmand et al. [29] for different Darcy numbers and good agreement is observed between the two. The second case study considers the particle-laden flow with transient convection heat transfer, where the fouling layer (EPFL) grows at the wall of the duct due to deposition of the particles. Fig. 7 shows the thermal efficiency drop of the duct with particle deposition compared with the experimental research of park et al. [17] on the real EGR cooler with $Re = 580$ that was operated for 40 min. As.

seen in Fig. 7, the results of the present study agree well with the experimental results of park et al. [17]. The thermal effectiveness of the duct is defined as follows:

$$\varepsilon_t = \frac{T_{in} - T_{b,out}}{T_{in} - T_w}$$

where ε_t is thermal effectiveness, $T_{b,out}$ is the outlet bulk temperature,

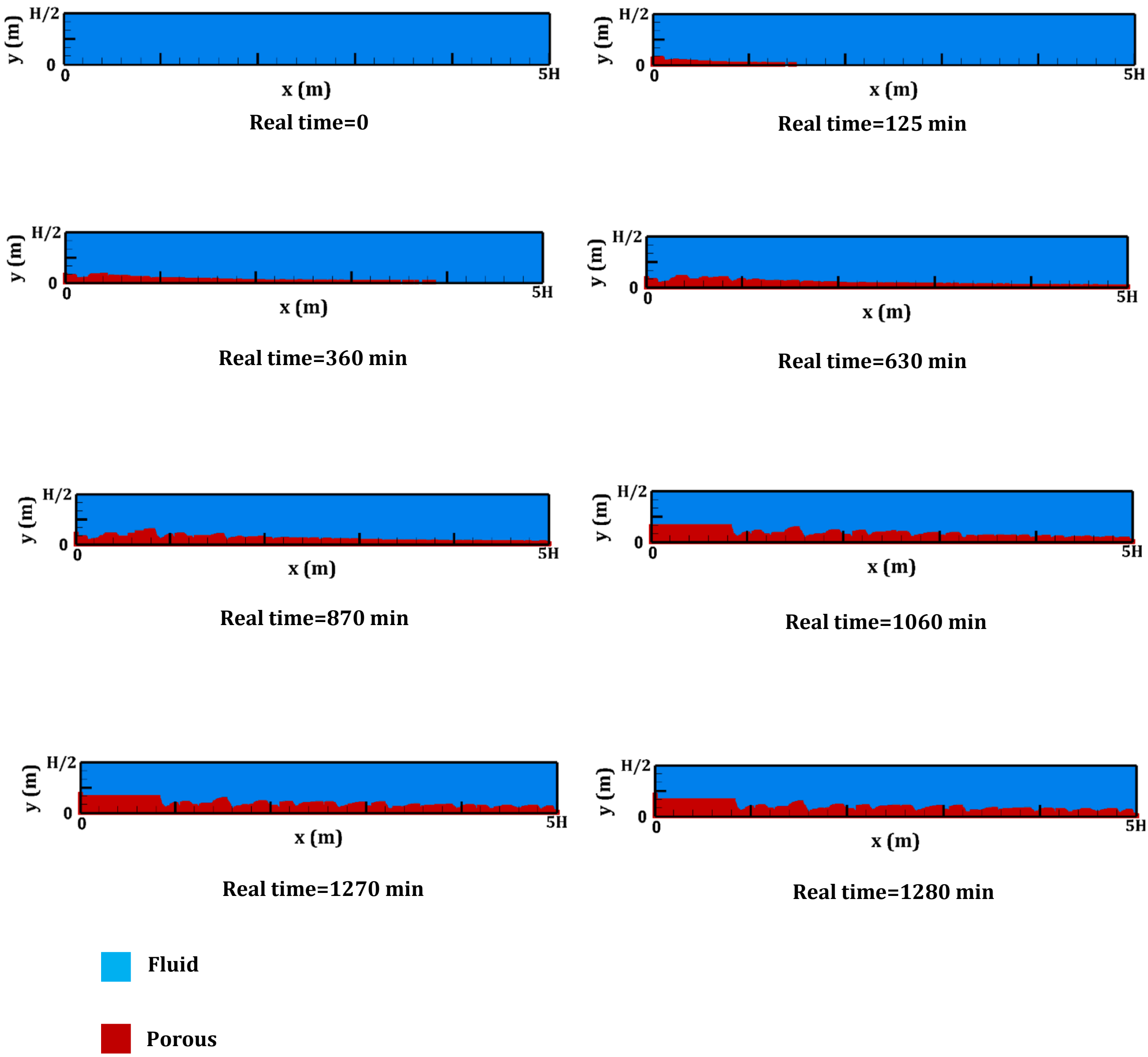

Fig. 8. EPFL generation in duct over the time for $Da = 10^{-4}$ and $Re = 100$.

and T_w is the wall temperature.

4. Result and discussion

In the present study, the lattice Boltzmann simulation of the particle-laden flow with laminar transient forced convection heat transfer in a parallel-plate duct, where deposition of particles and formation of the EPFL occurs, is investigated as shown in Fig. 1. In this paper, as the porous fouling layer builds up, the fluid flow and heat transfer within this EPFL is also simulated, which in turn affects the deposition behavior of particles due to a change that occurs in flow and temperature fields and consequently in the force experienced by the particles. In what follows, the effect of Darcy and Reynolds numbers on the time evolution of the fouling layer profile, flow field, Nusselt number ratio, and the time at which the steady fouling layer is achieved are presented.

4.1. Time evolution of the fouling layer profile, streamlines, and local Nusselt number

Fig. 8 presents the EPFL profile at different times for $Da = 10^{-4}$ and $Re = 100$. As seen in Fig. 8, the fouling layer grows with time in both longitudinal and transverse directions. It is obvious that at early times, the fouling layer mostly forms at the entrance region of the duct. This is due to the higher temperature gradient and, consequently, the higher thermophoresis force in that region, which pushes the particles towards the cold wall where they deposit and form the EPFL. This result has also been reported by other studies before [31,47]. As time goes by and EPFL becomes thicker, the thermal resistance against the convection heat transfer to the cold wall also increases, which reduces the temperature gradient, thereby reducing the thermophoresis force. This effect reduces the number of particles that deposit on the wall, and finally, the steady fouling layer (SFL) thickness is reached. An explanation for this phenomenon could be given based on the fact that two opposing effects are in play in the fouling phenomenon, one is the deposition of particles due to the thermophoresis force, and the other is reducing the

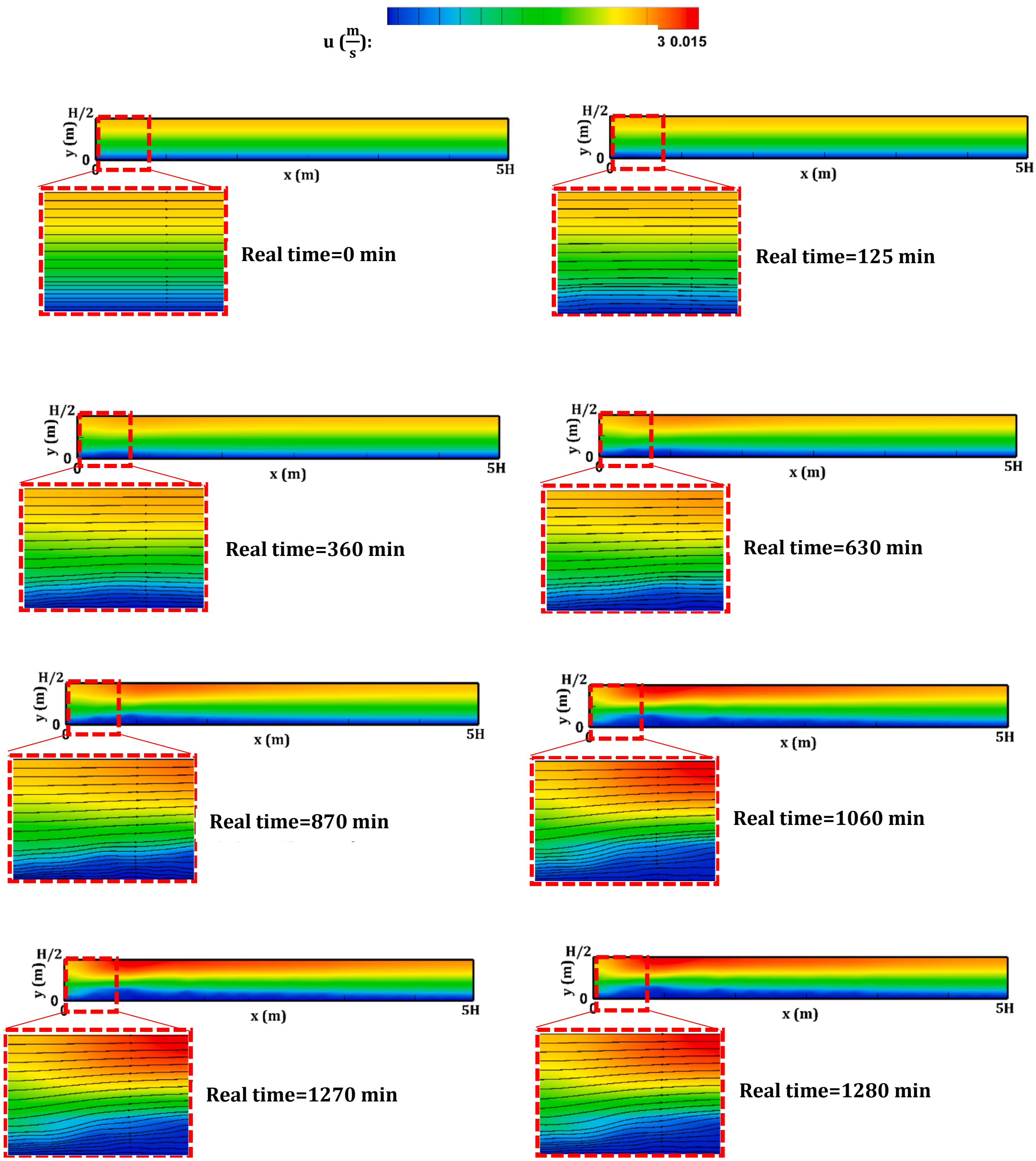

Fig. 9. Velocity contours and streamlines at different times for $Da = 10^{-4}$ and $Re = 100$.

thermophoresis force as a result of deposition and forming EPFL, which increases the thermal resistance, thereby reducing the temperature gradient as the driving force of the thermophoresis. From the hydrodynamic point of view, the formation of EPFL at the wall reduces the amount of flow that passes through this porous layer, which in turn increases the mass flow rate and velocity of the fluid in the core region. This increase in the velocity of the fluid enhances the drag force experienced by the particles (see equation (24)), which works against the thermophoresis force and elongates the path of the flying particles, thereby preventing them from being deposited throughout the duct.

Fig. 9 shows the effect of EPFL on the streamlines and velocity field at different times. It is seen from Fig. 9 that due to the formation of EPFL, the resistance to fluid flow within this porous layer increases, and the flow prefers to pass through the core region, which increases the velocity in that region.

Fig. 10 shows the local Nusselt for $Da = 10^{-4}$ and $Re = 100$ at different times. As shown in Fig. 10, the local Nusselt number declines along the duct length until it becomes nearly constant, where the thermal fully-developed condition is achieved. As time passes and the EPFL grows, the local Nusselt number shows slight fluctuations due to the fouling layer appearance. As shown in Fig. 10, the local Nusselt number drops more when the thickness of EPFL grows.

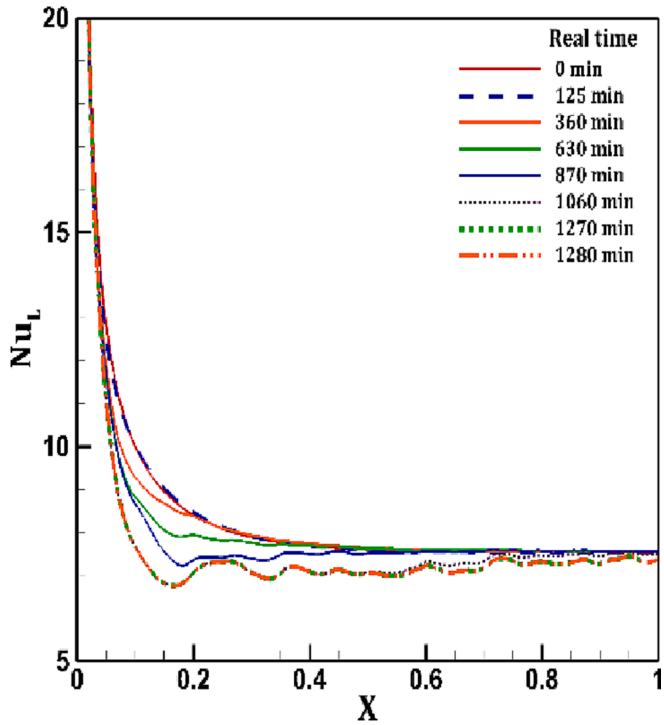

Fig. 10. Local Nusselt number for $Da = 10^{-4}$ and $Re = 100$.

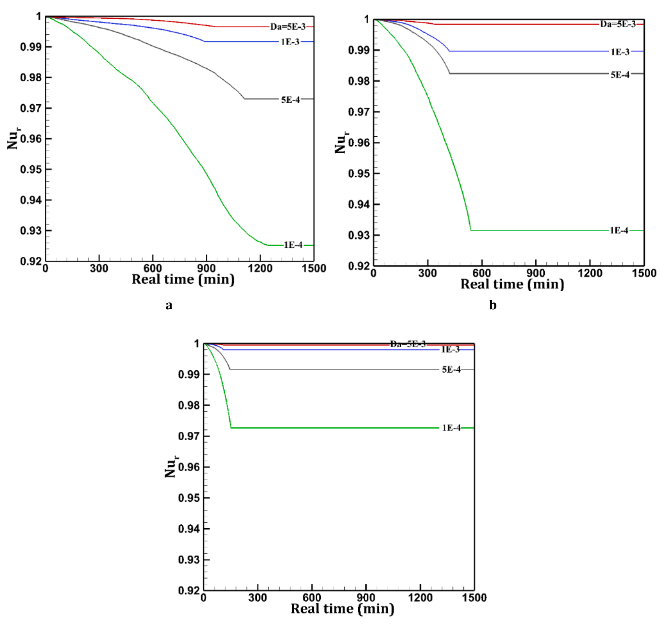

Fig. 11. The variations of the average Nusselt number ratio for different Darcy numbers and (a) $Re = 100$, (b) $Re = 200$, and (c) $Re = 400$.

4.2. Effect of Darcy and Reynolds numbers on the average Nusselt number ratio

In Fig. 11a, 11b, and 11c, the time variations of the average Nusselt number ratio, which is defined as the ratio of the average Nusselt number to the average Nusselt number of the clean duct ($Nu_r = Nu_{av}/Nu_{av}(t = 0)$) at each time is plotted for various Darcy and Reynolds numbers. As shown in Fig. 11a, 11b, and 11c, the EPFL with a smaller Darcy number has a higher reduction rate and causes a higher overall reduction in the Nu_r. For instance, at $Da = 10^{-4}$ and $Re = 100$ the relative overall reduction in Nu_r is calculated to be about 8% compared to a 6.5 % overall reduction which occurs for the case with $Da = 5 \times 10^{-3}$ and $Re = 100$. As seen in Fig. 11, the reduction in Nu_r stops at a certain time at which the fouling layer profile reaches a steady form called the SFL profile. The amount of this particular time, called the SFL time here, significantly depends on the Reynolds and Darcy numbers, as seen in Fig. 11. As discussed before, the opposing effects of particle deposition and reduction in thermophoresis due to the deposition of the particles and formation of the EPFL, can be thought as the reason behind this phenomenon of SFL formation. Moreover, it is seen from Fig. 11 that it takes more time for the case with a lower Darcy number to reach the SFL profile. In other words, the EPFL thickness is thicker when the Darcy number is lower. This phenomenon occurs due to the increase in temperature gradient for the EPFL with a lower Darcy number at the interface of the EPFL and clear fluid. This rise of temperature gradient causes the thermophoresis force to become higher for a lower Darcy number at the interface, so the particle deposition due to the thermophoresis lasts for longer times, which in turn increases the SFL time.

Fig. 12a and 12b show the average Nusselt number ratio for different Reynolds numbers at $Da = 10^{-4}$ and $Da = 5 \times 10^{-3}$. As shown in Fig. 12, the lower Reynolds number causes the highest overall reduction in Nu_r even though the rate of reduction is slower compared to higher Reynolds numbers. This is because, for the lower Reynolds numbers, the SFL time is higher, which compensates for the low reduction rates. This explanation is more obvious for the case with $Da = 10^{-4}$ where the overall reduction in Nu_r is higher compared to the case with $Da = 5 \times 10^{-3}$ for all Reynolds numbers examined here.

4.3. Effect of Darcy and Reynolds numbers on the thermal efficiency of the duct

Fig. 13a, 13b, and 13c illustrate the thermal efficiency (defined in equation (5)) reduction over time for the EGR duct. As seen in Fig. 13, the variation of the thermal efficiency with time shows the same behavior as Nu_r for different Reynolds and Darcy numbers. That is, the efficiency drop is higher for the lower Reynolds and Darcy numbers. The same goes for the SFL time, such that the lower the Reynolds and Darcy numbers are, the higher is the SFL time, where the fouling layer profile reaches its steady form. For example, less than 0.1% thermal efficiency drop in 900 mins is observed for $Re = 100$, $Da = 5 \times 10^{-3}$, whereas about 3.5% thermal efficiency drop in 1280 mins is observed for $Re = 100$, $Da = 10^{-4}$.

Fig. 14a and 14b show the effect of Reynolds number on the time variation of the thermal efficiency of the duct for $Da = 10^{-4}$ and $Da = 5 \times 10^{-3}$. As seen in Fig. 14, the Reynolds number has the same effect on the time variation of the thermal efficiency of the duct as Darcy number does. That is, the lower the Reynolds number, the higher is the overall reduction in thermal efficiency and the SFL time. It is also seen that the rate of reduction of thermal efficiency is lower for the lower Reynolds number. However, because the SFL time is higher for lower Reynolds numbers, the fouling layer has more time to develop, which causes a higher overall reduction in thermal efficiency. It also should be noted that before SFL time corresponding to the case with $Re = 400$, the higher Reynolds number offers more drop in thermal efficiency because of the higher reduction rate. For example, the amount of thermal efficiency reduction after 125mins is about 0.2% and 0.5%, respectively, for the cases with $Da = 5 \times 10^{-3}$, $Re = 100$ and $Da = 10^{-4}$, $Re = 400$.

4.4. The effect of Reynolds and Darcy numbers on the thermophoresis force

To shed some light on the reason behind the formation of the SFL and analyze the effect of Darcy and Reynolds numbers on the SFL time, Figs. 15-17 are plotted. Fig. 15 shows the y-distribution of the

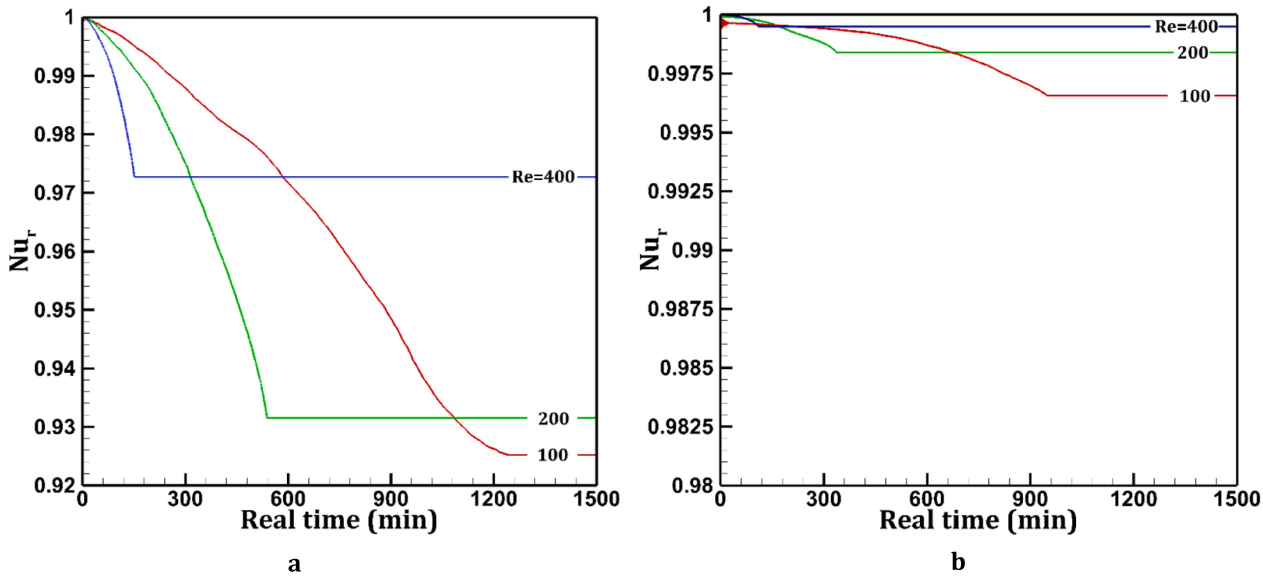

Fig. 12. The variations of the average Nusselt number ratio for different Reynolds numbers and (a) $Da = 10^{-4}$ and (b) $Da = 5 \times 10^{-3}$.

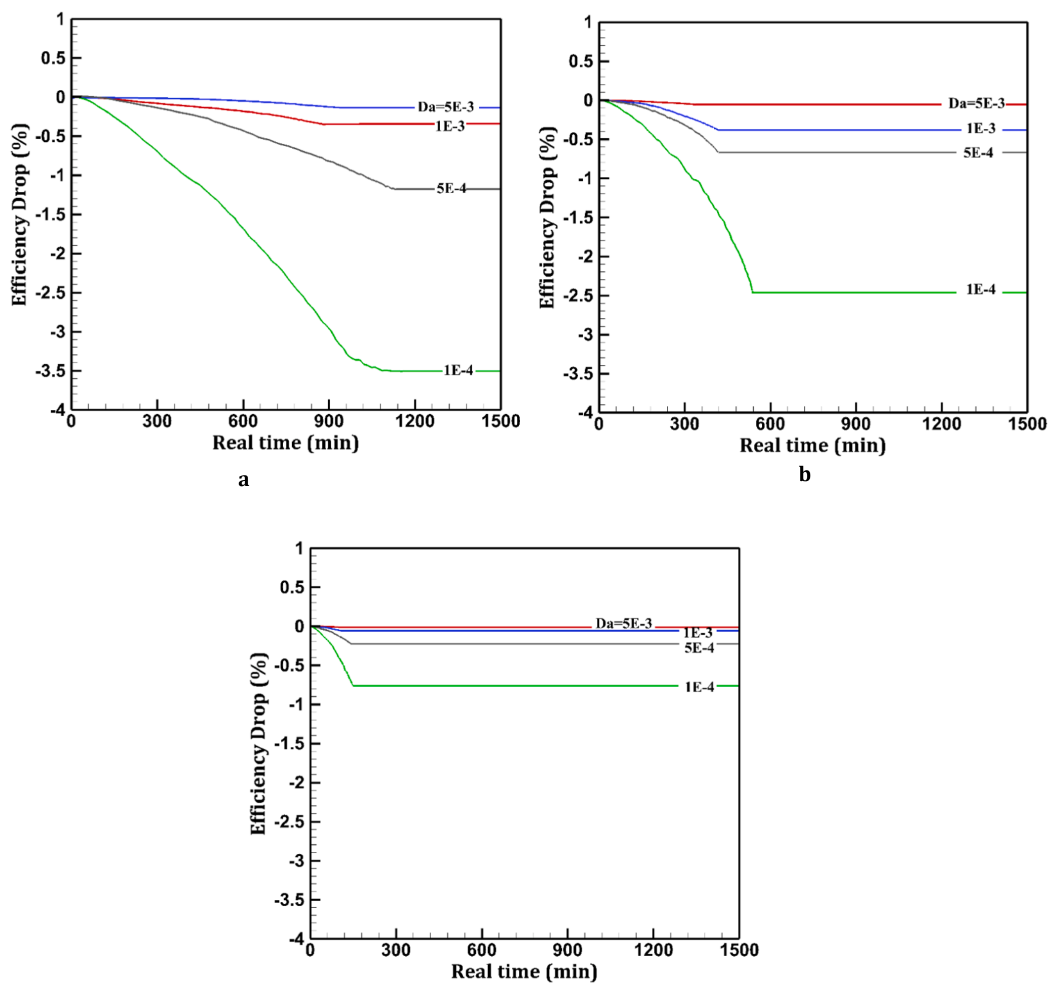

Fig. 13. The thermal efficiency reduction of the duct for various Darcy numbers and (a) $Re = 100$, (b) $Re = 200$, and (c) $Re = 400$.

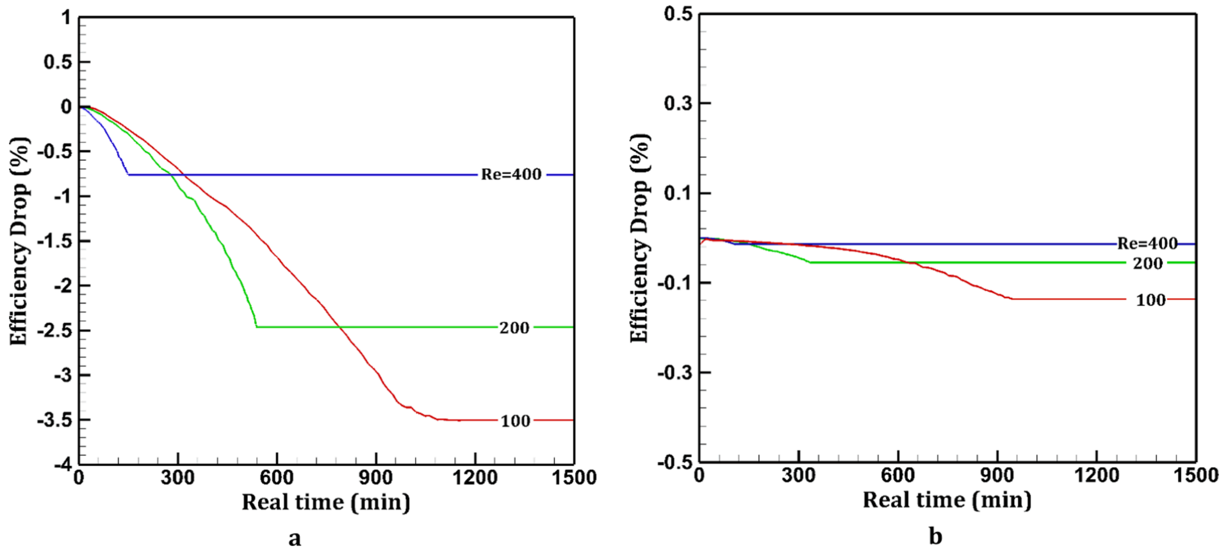

Fig. 14. The thermal efficiency reduction of the duct for various Reynolds numbers and (a) $Da = 10^{-4}$ (b) $Da = 5 \times 10^{-3}$.

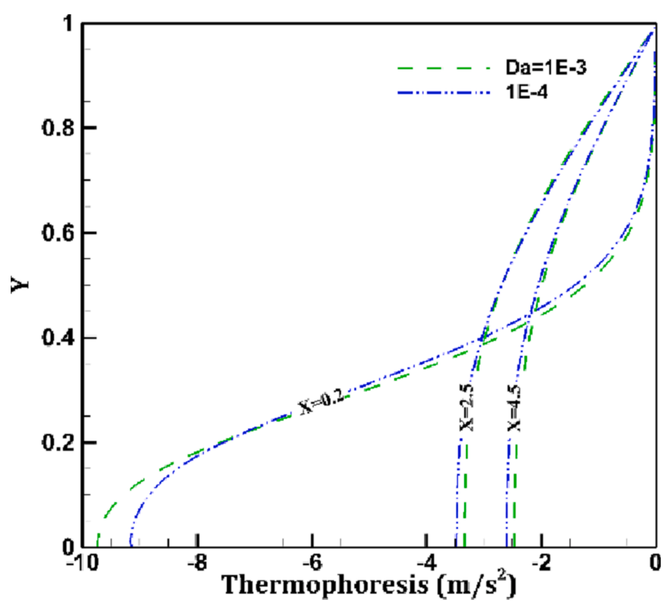

Fig. 15. The thermophoresis acceleration in different sections of the duct at $X = 0.2$, $X = 2.5$, and $X = 4.5$.

thermophoresis acceleration toward the wall at t = 500 min (the SFL time for the case with $Re = 100$ and $Da = 10^{-3}$) at three dimensionless locations along the duct, $X = 0.2$, 2.5, and 4.5 for $Da = 10^{-3}$ and 10^{-4}. As seen in Fig. 15, the amount of thermophoresis acceleration reduces in both longitudinal and transverse directions. This explains the formation of a thicker fouling layer at the entrance region of the duct, as seen in Fig. 8. Because thermophoresis is the dominant deposition force in EGR systems [12], at the entrance of the duct, the particles are more likely to deposit due to the high temperature gradient which results in a high thermophoresis force. As shown by Fig. 15, the effect of Darcy number on thermophoresis is more dominant in the vicinity of the wall where the EPFL is formed. This result is more obvious at $X = 0.2$ near the entrance of the duct.

Fig. 16 demonstrates the different fouling layer profiles for $Da = 10^{-4}$ and $Re = 100$, 200, and 400. As seen in Fig. 16, increasing the Reynolds number decreases the SFL thickness, especially in the entrance region of the duct. The SFL time also decreases when the Reynolds number increases. That is, the SFL time is about 151 min for $Da = 10^{-4}$, $Re = 400$ compared to 538 min for the case with $Da = 10^{-4}$ and $Re = 200$.

Fig. 17 shows the thermophoresis acceleration toward the wall for $Da = 10^{-4}$ and $Re = 100$, 200, and 400 at the SFL time. It is seen from Fig. 17 that the effect of the Reynolds number on the thermophoresis acceleration shows two opposing behaviors near the wall and in the core region. As shown in Fig. 17, near the wall, which is the EPFL region, the thermophoresis acceleration increases with increasing the Reynolds number, whereas far from the wall, which is the core or clear fluid region, this behavior reverses.

4.5. A correlation for the SFL time

The EGR coolers are designed to reduce the exhaust gas temperature before being recirculated into the engine. The fouling layer in such systems finally reaches a steady fouling layer (SFL) thickness during the operation period because of decreasing the thermophoresis force experienced by soot particles. So, in this section, a correlation is given for the SFL times in terms of Reynolds and Darcy numbers. Table 3 shows different SFL times for different Darcy numbers ($5 \times 10^{-3} \leq Da \leq 10^{-4}$) and Reynolds numbers ($100 \leq Re \leq 400$). It is seen from Table 3 that the SFL time decreases by increasing the Reynolds number, as discussed in previous sections. Also, changing the Darcy number causes the SFL time and deposition profile to change. Therefore, the following correlation in Table 3 is presented, which describes the SFL time (t_{SFL}) in terms of Reynolds and Darcy numbers:

5. Conclusion

Exhaust gas recirculation (EGR) coolers are developed to reduce the NOx emission in diesel engines by recirculating and cooling down the exhaust gas in such engines. However, the fouling in EGR coolers, which mainly occurs due to the thermophoretic force, has been shown to reduce their thermo-hydraulic performance over time. In the present study, the particle-laden flow with laminar transient forced convection heat transfer within an EGR cooler duct, where deposition of the particles occurs that results in the formation of an evolving porous fouling layer (EPFL) at the wall, is investigated by the lattice Boltzmann method. The results show that the coupled thermo-hydraulic effects of the EPFL and thermophoretic force eventually forms a steady fouling layer (SFL), similar to the well-documented asymptotic fouling behavior, even without considering the removal mechanism. Also, the following lists

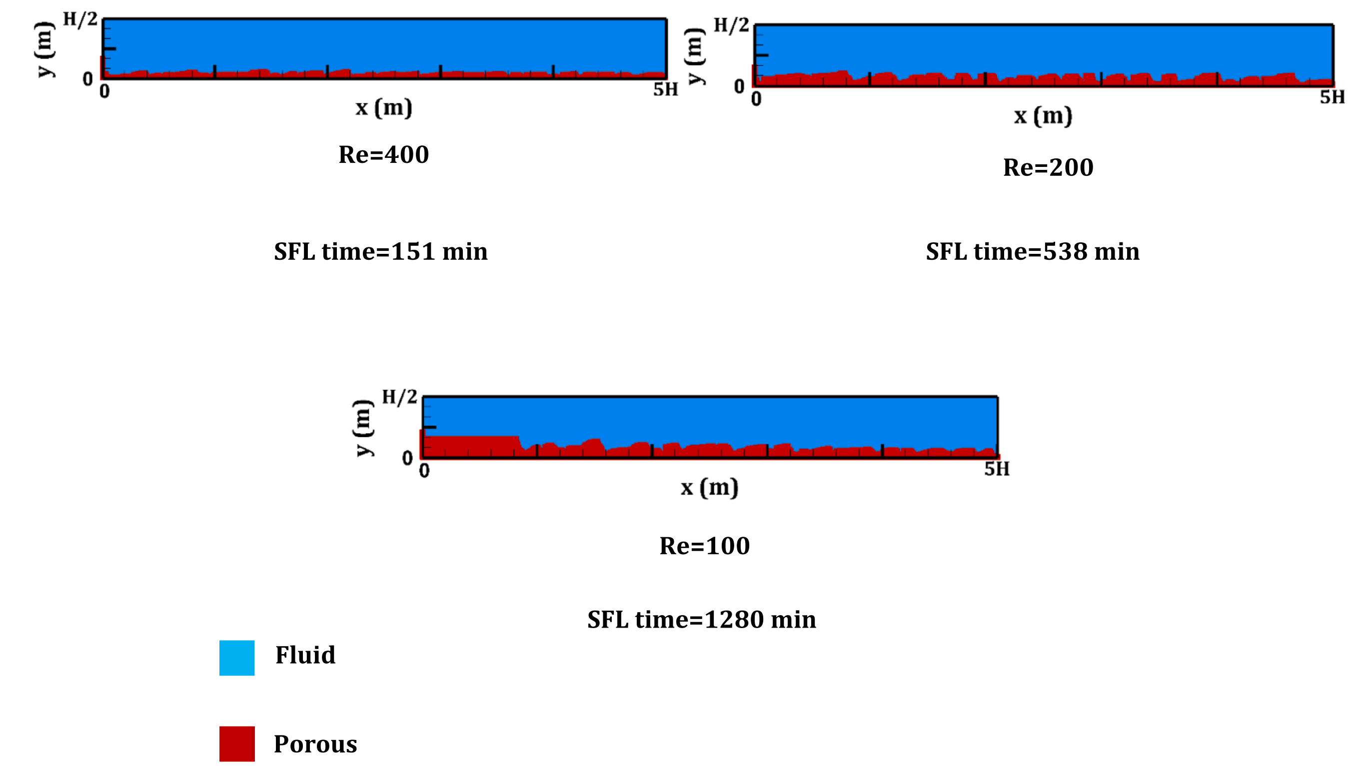

Fig. 16. The SFL profile and SFL time for $Da = 10^{-4}$ and different Reynolds numbers.

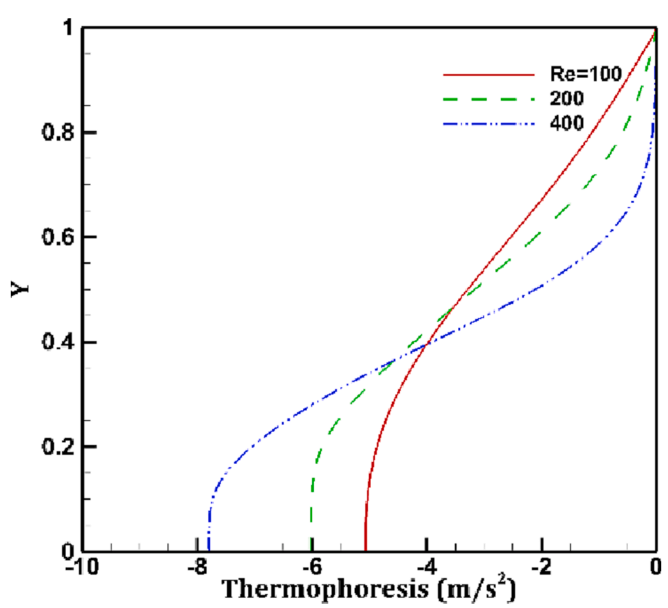

Fig. 17. The y-distribution of the thermophoresis acceleration at $X = 1$ for different Reynolds numbers.

the main results and conclusions extracted from this study:

1- The EPFL thickness increases by decreasing the Darcy and Reynolds numbers. Decreasing the Darcy number increases the EPFL thickness by increasing the thermophoresis force at the interface of the EPFL and homogeneous fluid medium.
2- The Nusselt number ratio (Nu_r) drops more for the lower Reynolds and Darcy numbers.
3- The thermal efficiency (ε_t) declines more by decreasing Reynolds and Darcy numbers.

Table 3
A correlation for the SFL time in terms of *Re* and *Da*.

	Da				Correlation formula	R^2
	10^{-4}	5×10^{-4}	10^{-3}	5×10^{-3}		
Re	t_{SFL}(min)				$t_{SFL} = (5.2Da^{-0.1}Re^{-1.5}) \times 10^5$	0.98
100	1280	1110	890	950		
200	538	421	415	336		
400	151	145	110	108		

4- The steady fouling layer (SFL) is finally reached due to decreasing the thermophoresis force as a result of forming the EPFL.
5- A correlation is proposed for the SFL time as $t_{SFL} = (5.2Da^{-0.1}Re^{-1.5}) \times 10^5$ in terms of Reynolds and Darcy numbers, which can be useful in designing such systems.

For the future work, the same research group is going to extend the current work to more realistic conditions, where turbulent flow regime is considered with taking into account the condensation of soluble organic materials (SOF) as well as the removal mechanism.

Declaration of Competing Interest

The authors declare that they have no known competing financial interests or personal relationships that could have appeared to influence the work reported in this paper.

Data availability

The research materials will be available upon a reasonable request.

References

[1] D. Qi, L. Ma, R. Chen, X. Jin, M. Xie, Effects of EGR rate on the combustion and emission characteristics of diesel-palm oil-ethanol ternary blends used in a CRDI diesel engine with double injection strategy, Appl. Therm. Eng. 25 (199) (2021), 117530.

[2] M. Choi, K. Mohiuddin, N. Kim, S. Park, Investigation of the effects of EGR rate, injection strategy and nozzle specification on engine performances and emissions of a single cylinder heavy duty diesel engine using the two color method, Appl. Therm. Eng. 5 (193) (2021), 117036.

[3] F.S. Anuar, K. Hooman, M.R. Malayeri, I.A. Abdi, Experimental study of particulate fouling in partially filled channel with open-cell metal foam, Exp. Therm Fluid Sci. 1 (110) (2020), 109941.

[4] M.S. Abd-Elhady, M.R. Malayeri, Mitigation of soot deposition in exhaust gas recirculation coolers using a spiral insert, Aerosol Sci. Tech. 48 (2) (2014) 184–192.

[5] K. Hooman, M.R. Malayeri, Metal foams as gas coolers for exhaust gas recirculation systems subjected to particulate fouling, Energ. Conver. Manage. 1 (117) (2016) 475–481.

[6] M.S. Abd-Elhady, M.R. Malayeri, Asymptotic characteristics of particulate deposit formation in exhaust gas recirculation (EGR) coolers, Appl. Therm. Eng. 28 (60) (2013) 96–104.

[7] M. Raza, L. Chen, F. Leach, S. Ding, A review of particulate number (PN) emissions from gasoline direct injection (GDI) engines and their control techniques, Energies 11 (6) (2018) 1417.

[8] K. Hong, J. Park, K. Lee, Experimental evaluation of SOF effects on EGR cooler fouling under various flow conditions, Int. J. Automot. Technol. 12 (6) (2011).

[9] V.C. Aiello, G. Kini, M.A. Staedter, S. Garimella, Investigation of fouling mechanisms for diesel engine exhaust heat recovery, Appl. Therm. Eng. 25 (181) (2020), 115973.

[10] A.S. Bika, A. Warey, D. Long, S. Balestrino, P. Szymkowicz, Characterization of soot deposition and particle nucleation in exhaust gas recirculation coolers, Aerosol Sci. Tech. 46 (12) (2012) 1328–1336.

[11] M.S. Abd-Elhady, T. Zornek, M.R. Malayeri, S. Balestrino, P.G. Szymkowicz, H. Müller-Steinhagen, Influence of gas velocity on particulate fouling of exhaust gas recirculation coolers, Int. J. Heat Mass Transf. 54 (4) (2011) 838–846.

[12] M. Abarham, J. Hoard, D. Assanis, D. Styles, E.W. Curtis, N. Ramesh, Review of soot deposition and removal mechanisms in EGR coolers, SAE Int. J. Fuels Lubr. 3 (1) (2010) 690–704.

[13] M.R. Malayeri, T. Zornek, S. Balestrino, A. Warey, P.G. Szymkowicz, Deposition of nanosized soot particles in various EGR coolers under thermophoretic and isothermal conditions, Heat Transfer Eng. 34 (8–9) (2013) 665–673.

[14] J. Hoard, M. Abarham, D. Styles, J.M. Giuliano, C.S. Sluder, J.M. Storey, Diesel EGR cooler fouling, SAE Int. J. Engines 1 (1) (2009) 1234–1250.

[15] S.H. Jang, S.J. Hwang, S.K. Park, K.S. Choi, H.M. Kim, Effects of PM fouling on the heat exchange effectiveness of wave fin type EGR cooler for diesel engine use, Heat Mass Transf. 48 (2012) 1081–1087.

[16] M.S. Abd-Elhady, M.R. Malayeri, H. Müller-Steinhagen, Fouling problems in exhaust gas recirculation coolers in the automotive industry, Heat Transfer Eng. 32 (3–4) (2011) 248–257.

[17] S. Park, K.S. Lee, J. Park, Parametric study on EGR cooler fouling mechanism using model gas and light-duty diesel engine exhaust gas, Energies 11 (11) (2018) 3161.

[18] C. Paz, E. Suárez, J. Vence, A. Cabarcos, Numerical modelling of fouling process in EGR system: a review, Environ. Issues Sustain. Develop. (2020).

[19] C. Paz, E. Suárez, A. Eirís, J. Porteiro, Development of a predictive CFD fouling model for diesel engine exhaust gas systems, Heat Transfer Eng. 34 (8–9) (2013) 674–682.

[20] M. Abarham, P. Zamankhan, J.W. Hoard, D. Styles, C.S. Sluder, J.M. Storey, M. J. Lance, D. Assanis, CFD analysis of particle transport in axi-symmetric tube flows under the influence of thermophoretic force, Int. J. Heat Mass Transf. 1 (61) (2013) 94–105.

[21] Z.X. Tong, M.J. Li, Y.L. He, H.Z. Tan, Simulation of real time particle deposition and removal processes on tubes by coupled numerical method, Appl. Energy 1 (185) (2017) 2181–2193.

[22] S.Z. Tang, Y.L. He, F.L. Wang, Q.X. Zhao, Y. Yu, On-site experimental study on fouling and heat transfer characteristics of flue gas heat exchanger for waste heat recovery, Fuel 15 (296) (2021), 120532.

[23] M.J. Lance, C.S. Sluder, H. Wang, J.M. Storey, Direct measurement of EGR cooler deposit thermal properties for improved. SAE 2009-01-1461, 2009.

[24] D. Poulikakos, M. Kazmierczak, Forced convection in a duct partially filled with a porous material, 1987.

[25] M.K. Alkam, M.A. Al-Nimr, M.O. Hamdan, Enhancing heat transfer in parallel-plate channels by using porous inserts, Int. J. Heat Mass Transf. 44 (5) (2001) 931–938.

[26] M.E. Kutay, A.H. Aydilek, E. Masad, Laboratory validation of lattice Boltzmann method for modeling pore-scale flow in granular materials, Comput. Geotech. 33 (8) (2006) 381–395.

[27] D. Chen, A. Riaz, V.C. Aute, R. Radermacher, A solid–liquid model based on lattice Boltzmann method for phase change material melting with porous media in cylindrical heat exchangers, Appl. Therm. Eng. 5 (207) (2022), 118080.

[28] H. Shokouhmand, F. Jam, M.R. Salimpour, Simulation of laminar flow and convective heat transfer in conduits filled with porous media using Lattice Boltzmann Method, Int. Commun. Heat Mass Transfer 36 (4) (2009) 378–384.

[29] H. Shokouhmand, F. Jam, M.R. Salimpour, The effect of porous insert position on the enhanced heat transfer in partially filled channels, Int. Commun. Heat Mass Transfer 38 (8) (2011) 1162–1167.

[30] A. Khoshnood, M. Maerefat, G. Imani, Lattice Boltzmann simulation of laminar forced convection in a parallel-plate duct with evolving porous layers at the walls, Int. Commun. Heat Mass Transfer 1 (136) (2022), 106204.

[31] M. Abarham, J. Hoard, D. Assanis, D. Styles, E.W. Curtis, N. Ramesh, C.S. Sluder, J. M. Storey, Modeling of thermophoretic soot deposition and hydrocarbon condensation in EGR coolers, SAE Int. J. Fuels Lubr. 2 (1) (2009) 921–931.

[32] A. Dimitriadis, I. Natsios, A. Dimaratos, D. Katsaounis, Z. Samaras, S. Bezergianni, K. Lehto, Evaluation of a hydrotreated vegetable oil (HVO) and effects on emissions of a passenger car diesel engine, Front. Mech. Eng. (4) (2018) 7.

[33] R. Kasper, J. Turnow, N. Kornev, Numerical modeling and simulation of particulate fouling of structured heat transfer surfaces using a multiphase Euler-Lagrange approach, Int. J. Heat Mass Transf. 1 (115) (2017) 932–945.

[34] L. Wang, L.P. Wang, Z. Guo, J. Mi, Volume-averaged macroscopic equation for fluid flow in moving porous media, Int. J. Heat Mass Transf. 1 (82) (2015) 357–368.

[35] Y. Mahmoudi, K. Hooman, K. Vafai (Eds.), Convective heat transfer in porous media, CRC Press, 2019 Nov 6.

[36] S.A. Khashan, A.M. Al-Amiri, M.A. Al-Nimr, Assessment of the local thermal non-equilibrium condition in developing forced convection flows through fluid-saturated porous tubes, Appl. Therm. Eng. 25 (10) (2005) 1429–1445.

[37] Q. Zou, X. He, On pressure and velocity boundary conditions for the lattice Boltzmann BGK model, Phys. Fluids 9 (6) (1997) 1591–1598.

[38] G. Zhao-Li, Z. Chu-Guang, S. Bao-Chang, Non-equilibrium extrapolation method for velocity and pressure boundary conditions in the lattice Boltzmann method, Chin. Phys. 11 (4) (2002) 366.

[39] D'Orazio A, Succi S. Boundary conditions for thermal lattice Boltzmann simulations. InComputational Science—ICCS 2003: International Conference, Melbourne, Australia and St. Petersburg, Russia, June 2–4, 2003 Proceedings, Part I 3 2003 (pp. 977-986). Springer Berlin Heidelberg.

[40] N. Zhang, X. Wei, Q. Yang, N. Li, E. Yao, Numerical simulation and experimental study of the growth characteristics of particulate fouling on pipe heat transfer surface, Heat Mass Transf. 8 (55) (2019) 687–698.

[41] Krishnamurthy, N, Investigation of Fouling in Wavy-Fin Exhaust Gas Recirculators, 2010, Virginia Tech.

[42] S.Z. Tang, F.L. Wang, Q. Ren, Y.L. He, Fouling characteristics analysis and morphology prediction of heat exchangers with a particulate fouling model considering deposition and removal mechanisms, Fuel 1 (203) (2017) 725–738.

[43] A. Bejan, Convection heat transfer, John Wiley & Sons, 2013.

[44] D.B. Kittelson, Engines and nanoparticles: a review, J. Aerosol Sci 29 (5–6) (1998) 575–588.

[45] J. Rissler, M.E. Messing, A.I. Malik, P.T. Nilsson, E.Z. Nordin, M. Bohgard, M. Sanati, J.H. Pagels, Effective density characterization of soot agglomerates from various sources and comparison to aggregation theory, Aerosol Sci. Tech. 47 (7) (2013) 792–805.

[46] M.K. Alkam, M.A. Al-Nimr, M.O. Hamdan, On forced convection in channels partially filled with porous substrates, Heat Mass Transf. 38 (4) (2002) 337–342.

[47] H. Sul, T. Han, M. Bieniek, J. Hoard, C.K. Kuan, D. Styles, The effects of temperature, shear stress, and deposit thickness on EGR cooler fouling removal mechanism-part 2, SAE Int. J. Mater. Manuf. 9 (2) (2016) 245–253.